

Cosimulation of Shifted-Frequency/Dynamic Phasor and Electromagnetic Transient Models of Hybrid LCC-MMC DC Grids on Integrated CPU–GPUs

Dewu Shu , Member, IEEE, Yingdong Wei , Member, IEEE, Venkata Dinavahi , Fellow, IEEE, Keyou Wang , Member, IEEE, Zheng Yan , Member, IEEE, and Xiaoqian Li , Member, IEEE

Abstract—To effectively capture interactions of large-scale ac–dc systems integrating line commutated converter (LCC) and modular multilevel converter (MMC) based multi-terminal dc grids, a numerically accurate and efficient simulation method is desirable. To achieve this objective, a cosimulation method is proposed in this article, where the target system is decoupled into the shifted-frequency phasor (SFP) subsystem, the dynamic phasor (DP) subsystem, and electromagnetic transient (EMT) subsystem, respectively. The MMCs are included in the SFP subsystem and implemented on massively paralleled graphics processing units (GPUs). Thus, the simulation efficiency is greatly improved by adopting a much larger time step, the model order reduction technique, and GPU acceleration. The LCCs are represented by DPs and are included in the DP subsystem. The majority of ac grids are covered in the EMT subsystem. Further, the interactions between SFP and EMT subsystems are reflected by the proposed multidomain transmission line model, which can produce instantaneous and phasor values simultaneously. The interface model between DP and EMT subsystems is modeled as a special controlled voltage and current circuit. Finally, the overall cosimulation method is realized by the respective SFP/DP and EMT models, among

which their interactions are reflected by the proposed interface models and the time sequences of simulations. The performance of the proposed method has been fully validated on a practical large-scale ac–dc system.

Index Terms—Dynamic phasor (DP) model, integrated CPU/graphics processing units (GPUs), interface model, line commutated converter (LCC), multiterminal dc (MTdc) grids, shifted-frequency phasor (SFP) model, voltage source converter (VSC).

I. INTRODUCTION

THE multiterminal dc (MTdc) grid, which combines the line commutated converter (LCC) and voltage source converter (VSC) topologies, has been considered as one of the most suitable solutions for flexible interconnections of multiarea ac systems [1]–[3]. In order to design the advanced control and protection systems for MTdc grids with the hybrid LCC and VSC topologies, as well as to analyze the interactions between large-scale ac and MTdc grids, an accurate and efficient simulation method, which can meticulously capture both electromechanical and electromagnetic dynamics, is highly desirable.

However, up to now, it is still unrealistic to simulate large-scale ac–dc grids integrating LCCs and modular multilevel converters (MMCs) by using electromagnetic transient (EMT) models. Actually, the computational burden is dramatically increased due to the following reasons.

- 1) *Computation increased by ac grids*: The number of nodes of the whole system is increased significantly by the expanding scale of the ac grids. Moreover, various nonlinear and frequency-dependent components add unexpected calculations to the system-level voltage equations.
- 2) *Computation increased by the MMCs*: Hundreds of submodules in each arm expand the node number sharply. In other words, the time-consuming calculations of the system-level admittance matrix should be refreshed during every switching occasion. Even worse, a much smaller time step (usually as small as 20–50 μ s) should be adopted to capture detailed switching actions of numerous power electronic devices.
- 3) *Computation increased by the LCC*: Although six nodes are added by one six-pulse LCC bridge in the system-level

Manuscript received November 11, 2018; revised February 13, 2019, April 8, 2019, June 9, 2019, and July 28, 2019; accepted August 6, 2019. Date of publication August 28, 2019; date of current version March 31, 2020. This work was supported in part by the Power Electronics Science and Education Development Program of Delta Group, in part by the Technology Projects of State Grid Corporation of China under Grant 52094017000W, in part by the National Natural Science Foundation of China under Grant 51877133, in part by the National Key Research and Development Program of China under Grant 2016YFB0900600, in part by the Shanghai Jiao Tong University Scientific and Technological Innovation Funds Power Company) under Grant 52097018000D, in part by Grant 2019 SJTU-KTH, and in part by the Shanghai Sailing Program under Grant 19YF1423500. (Corresponding author: Dewu Shu.)

D. Shu, K. Wang, and Z. Yan are with the High-Performance Simulation Center, Key Laboratory of Control and Power Transmission and Conversion, Department of Electrical Engineering, Shanghai Jiao Tong University, Shanghai 200240, China (e-mail: shudewu@sjtu.edu.cn; wangkeyou@sjtu.edu.cn; yanz@sjtu.edu.cn).

Y. Wei and X. Li are with Tsinghua University, Beijing 100084, China (e-mail: wyd@tsinghua.edu.cn; lixq-dee@tsinghua.edu.cn).

V. Dinavahi is with the Department of Electrical and Computer Engineering, University of Alberta, Edmonton, AB T6G1H9, Canada (e-mail: dinavahi@ualberta.ca).

Color versions of one or more of the figures in this article are available online at <http://ieeexplore.ieee.org>.

Digital Object Identifier 10.1109/TIE.2019.2937044

equations, the control and protection system of the LCC is very complicated, where hundreds of control nodes will be added in order to capture detailed dynamic responses of the LCC-HVdc. One of the typical examples is the Guanyinyan LCC-HVdc Project in China [4].

To improve the simulation efficiency from the aspect of modeling, several accelerated models based on model order reduction technique have been demonstrated. Specifically, several MMC accelerated models based on the circuit equivalence have been proposed, for instance, the switch-function model [5], the Thevenin equivalent model [6], and the arm equivalent model [7]. However, only simple topologies are tested on these models, such as the half-bridge or the full-bridge topology. A universal accelerated MMC model, which can be used for any submodule topology, is not covered in previous work. Unfortunately, the simulations of the large-scale ac grids as well as dc grids have to adopt such a unanimous and tiny time step, which increases the computational burden dramatically. Therefore, an accelerated and accurate MMC model for a universal submodule topology, which can adopt a much larger time step, is always desirable. Concerning the accelerated model of the LCC, the dynamic average model, such as the dynamic phasor (DP) model, is proposed to preserve the low-frequency dynamics but to improve the efficiency significantly [8], [9]. However, how to combine the efficient models of both the MMCs and the LCCs is not given in the previous work.

In addition to the model order reduction technique, the platform parallelism, such as using graphics processing units (GPUs), is another way to improve the computational efficiency. Various GPU-based applications have been adopted for power system computation, such as transient stability simulations [12], EMTs of wind farms [13], and transient stability constrained optimal power flows [14]. Therefore, in this article, the massive parallelism of many-core GPUs is utilized to further accelerate the simulations of the MMCs involving submodule level of details. The submodule equivalent models and the numerical algorithms have to be rewritten into the single instruction, multiple data format, where the calculations are decoupled into several independent and paralleled blocks, trying to improve the efficiency as much as possible.

To fully improve the simulation efficiency of large-scale ac-dc systems integrating LCC- and MMC-based MTdc grids, the cosimulation method combining the shifted-frequency phasor (SFP)/DP and EMT models is proposed. Its salient features include the following.

- 1) New SFP models based on the rotational matrix transformation are derived for the MMC with a universal submodule circuit. They can use a much larger time step and the calculations are fulfilled on GPUs; thus, the efficiency is dramatically improved.
- 2) The interactions between the SFP/DP and EMT subsystems are reflected and realized by the proposed interface models. The interface models between SFP and EMT subsystems can be represented by the multidomain transmission line model (MD-TLM) and the frequency-dependent multidomain transmission line model (FD-MD-TLM), where the latter can catch the high-frequency interactions

of interfacing. Moreover, the interface models between DP and EMT subsystems are represented by the controlled voltage and current circuits.

- 3) A new cosimulation framework is developed based on SFP/DP and EMT models, where the calculations are implemented on integrated CPU-GPUs and their interactions are reflected by the proposed interface models.

The rest of the article is organized as follows. Section II introduces the SFP model of the MMCs with a universal submodule topology. Section III elaborates the DP model of the LCC. Section IV illustrates the cosimulation method, including its architecture, the interface model, and the overall simulation procedure. Section V examines the performance of the proposed method on a practical ac-dc system in China. Section VI concludes this article.

II. SFP MODEL OF MMCs

A. Brief Introduction of Transformation-Based SFP Models

Typically, electrical variables in large-scale ac grids (assumed with fundamental frequency ω_s) can be represented by its SFP form [15], [16]

$$\begin{cases} u(t) = \hat{u}(t)e^{j\omega_s t} \\ \hat{u}(t) = u_I(t) + ju_Q(t) \end{cases} \quad (1)$$

where $\hat{u}(t)$ is the complex envelope of the time-domain signal $u(t)$, and ω_s denotes the fundamental frequency.

Suppose the dynamic equation of a system component is written as $du/dt = F(u, t)$, its dynamic equation in the SFP form can be derived as [17]

$$\frac{d\hat{u}}{dt} = \mathbf{F}(\hat{u}, t) - j\omega_s \hat{u}. \quad (2)$$

Decoupling into real and imaginary parts yields

$$\frac{d\hat{u}_{xy}}{dt} = \mathbf{F}(\hat{u}_{xy}, t) - \omega_s \mathbf{R} \left(-\frac{\pi}{2\omega_s} \right) \hat{u}_{xy} \quad (3)$$

where

$$\begin{aligned} \mathbf{F}(\hat{u}_{xy}, t) &= \begin{bmatrix} F(\hat{u}_x, t) \\ F(\hat{u}_y, t) \end{bmatrix}, \\ \mathbf{R}(t) &= \begin{bmatrix} \cos \omega_s t & -\sin \omega_s t \\ \sin \omega_s t & \cos \omega_s t \end{bmatrix}. \end{aligned} \quad (4)$$

In (3), $\hat{u}_{xy} = [\hat{u}_x \ \hat{u}_y]^T$, where \hat{u}_x and \hat{u}_y are the real and imaginary parts in the reference frame after Park's transform.

Adopting the trapezoidal algorithm, (3) is discretized as, eq. (5) shown at the bottom of the next page, where $\hat{u}(t)$, $\hat{f}(t)$ denote the state and the differential term, respectively, and Δt is the time step.

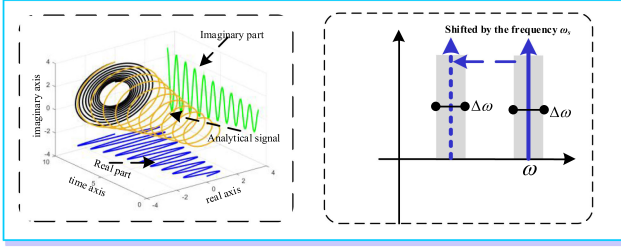


Fig. 1. Physical interpretation of shifted phasor modeling.

Based on (1) and (4), the SFPs can be transformed into time-domain signals

$$u(t) = \mathbf{R}(\Delta t)u(t - \Delta t) + \frac{\Delta t}{2} \begin{bmatrix} f(t) - \omega_s \mathbf{R}\left(-\frac{\pi}{2\omega_s}\right)u(t) + \mathbf{R}(\Delta t)f(t - \Delta t) \\ -\omega_s \mathbf{R}\left(\Delta t - \frac{\pi}{2\omega_s}\right)u(t - \Delta t) \end{bmatrix}. \quad (6)$$

The SFP concept is adopted hereafter to develop the models for MMC-based MTdc grid according to (6).

The physical interpretation of shifted phasor modeling is illustrated in Fig. 1. As can be seen, the frequency band of the dynamic system can be shifted by the frequency ω_s based on the Hilbert transform. The reason is due to the frequency shifting property of the Fourier coefficient. That is to say, a time-domain signal $x(t)$ multiplies $e^{\pm j\omega_s t}$ as $x(t)e^{\pm j\omega_s t}$, the two exponentials in the resulting integrand can be combined to get

$$x(t)e^{\pm j\omega_s t} \Leftrightarrow \mathbf{X}[j(\omega \mp \omega_s)] \quad (7)$$

where $\mathbf{X}[j\omega]$ denotes the Fourier coefficient of the time-domain signal $x(t)$. As shown in (1), when a time-domain signal $x(t)$ multiplies $e^{\pm j\omega_s t}$, the frequency band of $x(t)$ will be shifted by ω_s . As a result, the frequency band shifts from high-frequency band to the low-frequency band, where a larger time step can be used with improved efficiency and satisfied accuracy.

B. SFP Model of the Universal Submodule

Recently, new MMC topologies are emerging for low-voltage and high-voltage dc grids to add enhanced functionality to the converter, such as the fault ride-through and blocking/deblocking capabilities. Although several accelerated MMC models, such as the Thevenin equivalent model and the switch function model, have been proposed, the equivalent model has to be reformulated when the topology of the submodule is modified. Therefore, a universal submodule averaged model is necessary to simulate large-scale MMC-based MTdc grids.

For each topology of the MMC (see Fig. 1), such as the half-bridge SM sub-module, the full-bridge SM, and the clamped double SM, the equivalent circuit of the submodule can be de-

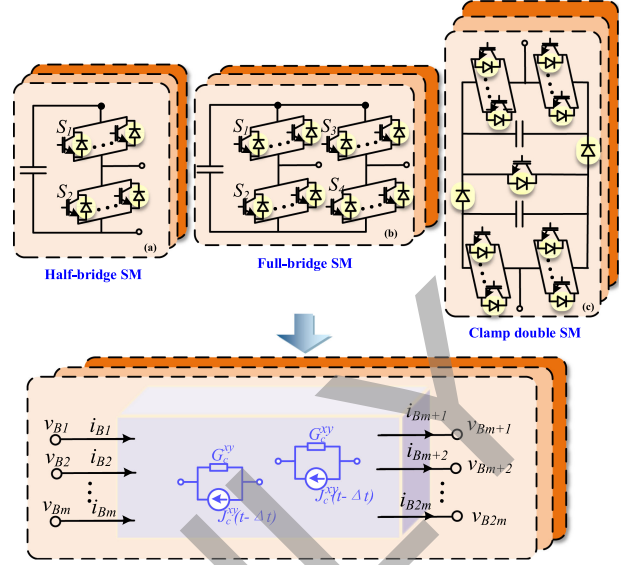


Fig. 2. Equivalent circuit model for the MMC.

derived by the combinations of the equivalent circuits of power electronic devices and the equivalent circuits of capacitors. According to (2)–(6), the dynamic equation of the capacitor in phasor domain is written as

$$\frac{d\hat{v}}{dt} = \frac{1}{C} \left[\hat{i} + \omega_s \mathbf{R}\left(-\frac{\pi}{2\omega_s}\right) C \hat{v} \right] \quad (8)$$

where $\hat{v}(t)$ and $\hat{i}(t)$ denote the capacitor voltages and currents in phasor domain, respectively.

After some manipulations, variables in phasor domain are transferred back to time domain

$$i^{xy}(t) = G_c^{xy} v^{xy}(t) + J_c^{xy}(t - \Delta t) \quad (9)$$

where

$$\begin{cases} G_c^{xy} = \frac{2C}{\Delta t} \otimes I_{2 \times 2} - \omega_s \mathbf{R}\left(-\frac{\pi}{2\omega_s}\right) C \\ J_c^{xy}(t - \Delta t) = \frac{2C}{\Delta t} \otimes I_{2 \times 2} v^{xy}(t - \Delta t) \\ + \mathbf{R}(\Delta t) i^{xy}(t - \Delta t) + \omega_s \mathbf{R}\left(\Delta t - \frac{\pi}{2\omega_s}\right) C i^{xy}(t - \Delta t) \end{cases}. \quad (10)$$

As shown in Fig. 2, the SFP model of a universal submodule is represented as a multiport Thevenin equivalent circuit. The concrete procedure is as follows.

Step 1: Derive the component level SFP models: The power electronic devices are represented as $R_{\text{on}}/R_{\text{off}}$ resistance model. Therefore, power electronic devices only contribute to elements of the conductance matrix. The SFP model of capacitors can be referred to as (9) and (10).

Step 2: Formulate the system-level conductance matrix and the equivalent current. According to the nodal analysis

$$\frac{\hat{u}(t) - \hat{u}(t - \Delta t)}{\Delta t} = \frac{\hat{F}(t) - \omega_s \mathbf{R}\left(-\frac{\pi}{2\omega_s}\right)\hat{u}(t) + \hat{F}(t - \Delta t) - \omega_s \mathbf{R}\left(-\frac{\pi}{2\omega_s}\right)\hat{u}(t - \Delta t)}{2} \quad (5)$$

approach, the system-level conductance is calculated as

$$\mathbf{G}^{xy} = \sum_{i=1} M_i^T \mathbf{G}_{ci}^{xy} M_i + \sum_{j=1} M_j^T \mathbf{G}_{ej}^{xy} M_j \quad (11)$$

where \mathbf{G}_{ci}^{xy} denotes the conductance of the i th capacitor; \mathbf{G}_{ej}^{xy} denotes the conductance of the j th power electronic devices; and M_i and M_j are the incidence vector, which reflects the connected buses of the component. They are of the form like $[0 \dots 1 \dots -1 \dots 0]^T$, with integers 1 and -1 denoting the start and end node of the corresponding branch, respectively [18].

Similarly, the equivalent current of the whole system is calculated as

$$\mathbf{J}^{xy}(t - \Delta t) = \sum_{i=1} M_i^T \mathbf{J}_{ci}^{xy}(t - \Delta t) M_i \quad (12)$$

where $\mathbf{J}_{ci}^{xy}(t - \Delta t)$ is the equivalent current of the i th capacitor.

Therefore, the nodal voltage equation of the whole system in Fig. 1 can be formulated as

$$\begin{bmatrix} \mathbf{G}_{BB}^{xy} & \mathbf{G}_{BN}^{xy} \\ \mathbf{G}_{NB}^{xy} & \mathbf{G}_{NN}^{xy} \end{bmatrix} \begin{bmatrix} \mathbf{v}_B^{xy}(t) \\ \mathbf{v}_N^{xy}(t) \end{bmatrix} = \begin{bmatrix} \mathbf{J}_B^{xy}(t - \Delta t) \\ \mathbf{J}_N^{xy}(t - \Delta t) \end{bmatrix} \quad (13)$$

where B and N denote the boundary buses and internal buses, respectively, of the universal submodule.

Step 3: The boundary buses are only retained by Gaussian elimination

$$\mathbf{G}_{eq} \mathbf{v}_B^{xy}(t) = \mathbf{J}_{eq}^{xy}(t - \Delta t) \quad (14)$$

where

$$\begin{cases} \mathbf{G}_{eq} = \mathbf{G}_{BB}^{xy} - \mathbf{G}_{BN}^{xy} [\mathbf{G}_{NN}^{xy}]^{-1} \mathbf{G}_{NB}^{xy} \\ \mathbf{J}_{eq}^{xy}(t - \Delta t) = \mathbf{J}_B^{xy}(t - \Delta t) - \mathbf{G}_{BN}^{xy} [\mathbf{G}_{NN}^{xy}]^{-1} \mathbf{J}_N^{xy}(t - \Delta t) \end{cases} \quad (15)$$

where \mathbf{G}_{eq} and $\mathbf{J}_{eq}^{xy}(t - \Delta t)$ denote and constitute the conductance matrix and the equivalent current vector of the universal submodule.

C. SFP Model of the MMC

The aggregate SFP model of the MMC can be derived as an overall Thevenin equivalent circuit by adding all the SFP models of each submodule together

$$\begin{aligned} \begin{bmatrix} v_{arm}^x(t) \\ v_{arm}^y(t) \end{bmatrix} &= \mathbf{R}_{eq} \sum \begin{bmatrix} i_{arm}^x(t) \\ i_{arm}^y(t) \end{bmatrix} + v_{eq}^{\sum}(t - \Delta t) \\ &= \sum_{k=1}^N S_k \left\{ \mathbf{R}_{eq,k} \begin{bmatrix} i_{arm}^x(t) \\ i_{arm}^y(t) \end{bmatrix} + v_{eq,k}^{xy}(t - \Delta t) \right\} \end{aligned} \quad (16)$$

where $S_k, k = 1, 2, \dots, N$, is the switch function, denoting whether the submodule is bypassed or not; and $\mathbf{R}_{eq,k}$ and $v_{eq,k}^{xy}(t - \Delta t)$ are the Thevenin equivalent resistance and voltages of the k th submodule, respectively, which can be calculated by

$$\begin{cases} \mathbf{R}_{eq,k} = 1/\mathbf{G}_{eq,k} \\ v_{eq,k}^{xy}(t - \Delta t) = \mathbf{J}_{eq,k}^{xy}(t - \Delta t)/\mathbf{G}_{eq,k} \end{cases} \quad (17)$$

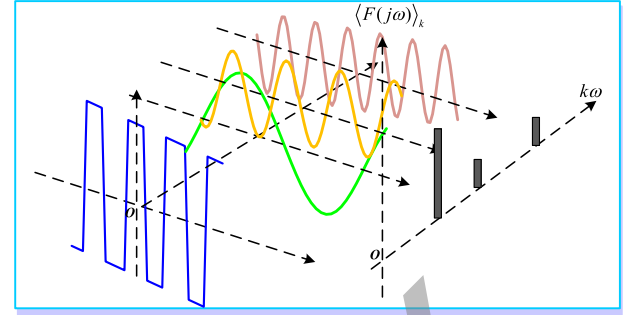


Fig. 3. Physical interpretation of DP modeling.

where $\mathbf{G}_{eq,k}$ and $\mathbf{J}_{eq,k}^{xy}(t - \Delta t)$ are the conductance matrix and the equivalent current vector of the k th submodule, respectively, which can be referred to (14) and (15).

III. DP MODEL OF LCC CONVERTER

A. DP Concept

The concept of DP is illustrated in Fig. 3, where the frequency band of dynamic components is divided into equal intervals. The signal $x(\tau)$, $\tau \in (t - T, t]$, with the period T is expressed in the form of time-varying Fourier series [10], [11], i.e.,

$$\begin{cases} x(\tau) = \sum_{k=-\infty}^{\infty} \hat{\mathbf{x}}_k(t) e^{jk\omega\tau} \\ \hat{\mathbf{x}}_k(t) = \frac{1}{T} \int_{t-T}^t x(\tau) e^{-jk\omega\tau} d\tau \end{cases} \quad (18)$$

where $\omega = 2\pi/T$, and $\hat{\mathbf{x}}_k(t)$ is the k th DP of $x(\tau)$. When the time window with the period of T moves along the time axes, the DPs are changed with the time t .

Two important features, i.e., the product feature and the differential feature of the DP, are given as

$$\begin{cases} (\hat{\mathbf{x}}\hat{\mathbf{y}})_k = \sum_i \hat{\mathbf{x}}_{k-i} \hat{\mathbf{y}}_i \\ \frac{d}{dt} \hat{\mathbf{x}}_k = \left(\frac{d\hat{\mathbf{x}}}{dt} \right)_k - jk\omega \hat{\mathbf{x}}_k \end{cases} \quad (19)$$

Based on (18) and (19), the corresponding DP models of power system components can be derived. For a component modeled with its algebraic differential equation

$$\begin{cases} \frac{dx}{dt} = Ax(t) + Bv(t) \\ i(t) = Cx(t) + Dv(t) \end{cases} \quad (20)$$

where x represents the state variables, $v(t)$ and $i(t)$ refer to the voltage and the current of the component, respectively, and A, B, C, D are the parameters.

According to (18) and (19), the corresponding DP model of (20) can be derived as

$$\begin{cases} \frac{d\hat{\mathbf{x}}_k(t)}{dt} = A_k \hat{\mathbf{x}}_k(t) + B \hat{\mathbf{v}}_k(t) \\ \hat{\mathbf{i}}_k(t) = C \hat{\mathbf{x}}_k(t) + D \hat{\mathbf{v}}_k(t) \end{cases} \quad (21)$$

where $A_k = A - jk\omega I$.

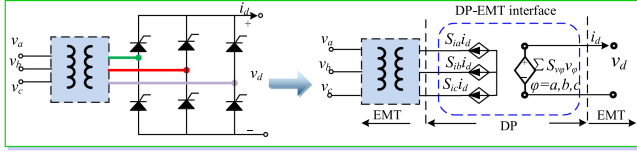


Fig. 4. DP model of LCC converter.

By discretizing (21) based on the trapezoidal algorithm, (21) can be calculated in the DP form as

$$\hat{\mathbf{x}}_k(t) = \left(\frac{2}{\Delta t} - A_k \right)^{-1} \times \left[\left(\frac{2}{\Delta t} + A_k \right) \hat{\mathbf{x}}_k(t - \Delta t) + B \hat{\mathbf{v}}_k(t) + B \hat{\mathbf{v}}_k(t - \Delta t) \right]. \quad (22)$$

B. DP Modeling of the LCC

In order to capture EMTs of the LCC, its DP model is derived hereafter for efficient simulations. As shown in Fig. 4, a six-pulse thyristor bridge converter is the basic building block of the LCC-HVdc. Different LCC-HVdc systems, such as monopolar and bipolar structures, can be obtained by properly arranging such building blocks along with transformers and grounding schemes. The relationships between dc quantities and ac quantities for a six-pulse LCC bridge can be derived by switch functions as [9]

$$v_d = v_a S_{v_a} + v_b S_{v_b} + v_c S_{v_c} \quad (23)$$

$$\begin{cases} i_a = i_d S_{i_a} \\ i_b = i_d S_{i_b} \\ i_c = i_d S_{i_c} \end{cases} \quad (24)$$

where v_a, v_b, v_c and i_a, i_b, i_c are the three-phase voltages and currents, respectively, of the ac side of the converter; V_d and i_d are the dc voltage and current, respectively; and $S_{v_a}, S_{v_b}, S_{v_c}$ and $S_{i_a}, S_{i_b}, S_{i_c}$ represent the switch functions of voltages and currents, respectively. The switch functions of voltages and currents can be represented by their DPs as

$$\begin{cases} S_{v_\varphi} = \sum_{k=-N}^N \langle S_{v_\varphi} \rangle_k e^{jk\omega t}, \varphi = a, b, c \\ S_{i_\varphi} = \sum_{k=-N}^N \langle S_{i_\varphi} \rangle_k e^{jk\omega t}, \varphi = a, b, c \end{cases} \quad (25)$$

where N denotes the order of DPs; and $\langle S_{v_\varphi} \rangle_k, \langle S_{i_\varphi} \rangle_k$ are their k th-order DPs.

As shown in Fig. 4, the DP model of the LCC is modeled as a special controlled voltage and current circuit. Therein, the dc current i_d and the ac voltages $v_\varphi, \varphi = a, b, c$, are set as input signals. The dc voltage v_d and the ac currents $i_\varphi, \varphi = a, b, c$, are the corresponding output signals. Suppose the dc current contains the dc components and the second harmonics, the ac voltages and dc currents can be derived by DPs as

$$\begin{cases} v_\varphi = \langle v_\varphi \rangle_1 e^{j\omega t} + \langle v_\varphi \rangle_{-1} e^{-j\omega t}, \varphi = a, b, c \\ i_d = \langle i_d \rangle_0 + \langle i_d \rangle_2 e^{j2\omega t} + \langle i_d \rangle_{-2} e^{-j2\omega t} \end{cases} \quad (26)$$

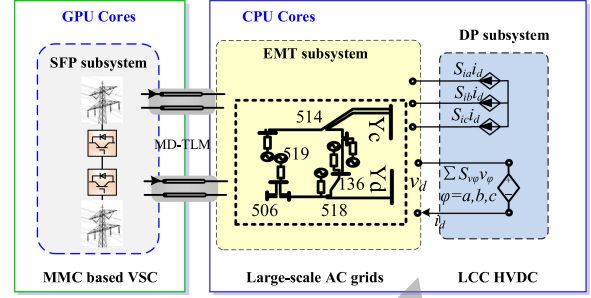


Fig. 5. Network partitioning of the whole system.

where $\langle v_\varphi \rangle_1, \langle v_\varphi \rangle_{-1}$ are the first-order DPs of ac voltages; and $\langle i_d \rangle_0, \langle i_d \rangle_2, \langle i_d \rangle_{-2}$ are the zeroth-order and second-order DPs of the dc current.

According to (17) and (18), DPs of dc voltages and ac currents are calculated by

$$\begin{aligned} \langle v_d \rangle_0 &= \sum_{\varphi=a,b,c} \langle v_\varphi \rangle_{-1} \langle S_{v_\varphi} \rangle_1 + \sum_{\varphi=a,b,c} \langle v_\varphi \rangle_1 \langle S_{v_\varphi} \rangle_{-1} \\ \langle v_d \rangle_2 &= \sum_{\varphi=a,b,c} \langle v_\varphi \rangle_{-1} \langle S_{v_\varphi} \rangle_3 + \sum_{\varphi=a,b,c} \langle v_\varphi \rangle_1 \langle S_{v_\varphi} \rangle_{-3} \\ \langle v_d \rangle_{-2} &= \sum_{\varphi=a,b,c} \langle v_\varphi \rangle_{-1} \langle S_{v_\varphi} \rangle_{-1} + \sum_{\varphi=a,b,c} \langle v_\varphi \rangle_1 \langle S_{v_\varphi} \rangle_{-3} \end{aligned} \quad (27)$$

$$\begin{aligned} \langle i_\varphi \rangle_1 &= \langle i_d \rangle_{-2} \langle S_{i_\varphi} \rangle_3 + \langle i_d \rangle_0 \langle S_{i_\varphi} \rangle_1 + \langle i_d \rangle_2 \langle S_{i_\varphi} \rangle_{-1} \\ \langle i_\varphi \rangle_{-1} &= \langle i_d \rangle_{-2} \langle S_{i_\varphi} \rangle_1 + \langle i_d \rangle_0 \langle S_{i_\varphi} \rangle_{-1} + \langle i_d \rangle_2 \langle S_{i_\varphi} \rangle_{-3} \end{aligned} \quad (28)$$

where values of $\langle S_{i_\varphi} \rangle_k, \langle S_{v_\varphi} \rangle_k, k = 0, \pm 1, \pm 2, \pm 3$, are the functions of overlap angle, which can be analytically calculated [9]. Other values can be derived based on the fast Fourier transform technique.

Finally, the instantaneous values of dc voltages and ac currents are obtained as

$$\begin{aligned} v_d &= \langle v_d \rangle_0 + \langle v_d \rangle_2 e^{j2\omega t} + \langle v_d \rangle_{-2} e^{-j2\omega t} \\ i_\varphi &= \langle i_\varphi \rangle_1 e^{j\omega t} + \langle i_\varphi \rangle_{-1} e^{-j\omega t}, \varphi = a, b, c. \end{aligned} \quad (29)$$

IV. COSIMULATION OF SFP/DP AND EMT MODELS

The SFP/DP models derived in the previous section are used to accelerate the simulation speed of the MMCs and the LCCs, respectively. To take full advantages of SFP and DP models in improving the efficiency of large-scale ac–dc systems, the concept of the cosimulation that combines the SFP/DP and EMT models is proposed. As shown in Fig. 5, the idea of the proposed cosimulation method is to partition the target system into SFP, DP, and EMT subsystems, represented by our developed SFP models, DP models, and traditional EMT models, respectively. Specifically, the large-scale ac grids are included in the EMT subsystem in order to capture the frequency-dependent dynamics of transmission lines and nonlinear dynamics of generators. The MMCs are included in the SFP subsystem, where each converter is modeled by the proposed SFP model. One of the salient advantages of the SFP model is that it can adopt a

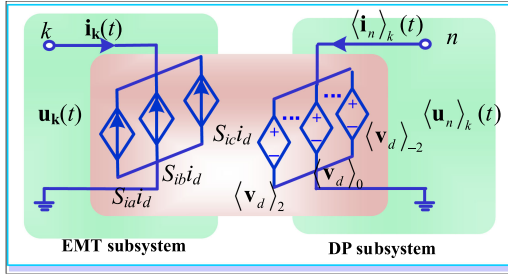


Fig. 6. Interface model between DP and EMT subsystems.

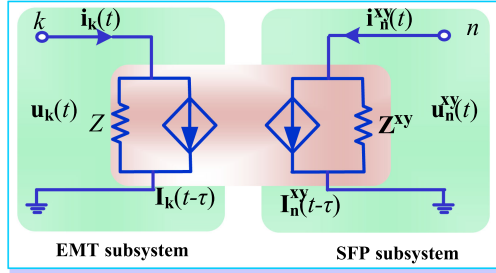


Fig. 7. Structure of the MD-TLM.

much larger time step so as to improve the simulation efficiency effectively. Actually, the simulation efficiency of the SFP subsystem is greatly improved by adopting a much larger time step, the model order reduction technique, and GPU acceleration. Besides, the LCCs are included in the DP subsystem, where each LCC is represented in a more efficient model, or its DP model according to Section III.

The wide frequency band interactions between different subsystems are captured and reflected by the proposed interface models. Specifically, the interface model between EMT and DP subsystems is represented as a controlled voltage and current circuit in the forms of DPs and time-domain variables. The interface model between SFP and EMT subsystems is represented by our proposed MD-TLM.

A. Interface Model Between DP and EMT Subsystems

The interface model between DP and EMT subsystems is depicted in Fig. 6. As can be seen, the interface models in EMT subsystem are represented by the controlled current source, values of which are calculated according to (28). On the other hand, the interface models in the DP subsystem are represented as the controlled voltage sources in the DP form, values of which are derived according to (27). Variables in the EMT subsystems are represented in the time-domain form, whereas those in DP subsystems are represented in their DP form.

B. Interface Model Between SFP and EMT Subsystems

Two types of interface model between SFP and EMT subsystems are detailed with/without the frequency-dependent dynamics of interface models: 1) the MD-TLM based on the Bergeron model, and 2) the FD-MD-TLM.

1) MD-TLM Based on the Bergeron Model: As shown in Fig. 7, the MD-TLM is represented as a dual Norton equivalent circuit, or a paralleled impedance and a controlled current source

with a time delay (traveling time) τ . Since the time delay τ is usually not an integer multiple of the time step, historical values on either side should be interpolated to obtain their accurate values in time domain and phasor domain, respectively.

The equivalent source in the EMT subsystem $I_k(t - \tau)$ is calculated as

$$I_k(t - \tau) = -Z^{-1}u_n(t - \tau) - i_n(t - \tau) \quad (30)$$

where $u_n(t - \tau)$ and $i_n(t - \tau)$ are instantaneous interface voltages and currents, respectively, of node n in the EMT subsystems.

Then, the equivalent current vector $\mathbf{I}_n^{xy}(t - \tau)$ in the SFP subsystem with the time delay of τ is calculated by

$$\begin{aligned} \mathbf{I}_n^{xy}(t - \tau) = & -[\mathbf{u}_k^{xy}(t - \tau)\mathbf{R}(-\theta)]/[Z \otimes I_{2 \times 2}] \\ & - \mathbf{i}_k^{xy}(t - \tau)\mathbf{R}(-\theta) \end{aligned} \quad (31)$$

where $\tau = l/v$, $\theta = \omega l/v$, $Z = \sqrt{L/C}$; and \otimes denotes the Kronecker product, or the element-by-element multiplication.

According to (31), in order to calculate the current injection at node n , instantaneous quantities at the EMT side [i.e., $u_k(t - \tau)$, $i_k(t - \tau)$] should be converted to their SFP-based quantities. Similarly, to determine the current injection at node k using (30), the SFP-based quantities at node n should be converted to instantaneous values. It should be noted that quantities at the time $t - \tau$ should be estimated by linear interpolations in phasor domain and time domain between $[t - (k - 1)\Delta t, t - k\Delta t]$ in order to obtain their accurate values, where $k = \lceil \tau/\Delta t \rceil + 1$. Therefore, bidirectional signal conversion is required to update parameters of the proposed MD-TLM.

2) Frequency-Dependent Multidomain Transmission Line Model: The FD-MD-TLM is given in Fig. 8. The core issue for the FD-MD-TLM is how to update the frequency-dependent characteristic impedance and the equivalent current time domain and phasor domain, respectively.

We consider a frequency-dependent interface transmission line of length l which, in the frequency domain, is characterized by the per-unit-length parameters of series impedance $\mathbf{Z}(s) = \mathbf{R}(s) + s\mathbf{L}(s)$ and shunt admittance $\mathbf{Y}(s) = \mathbf{G}(s) + s\mathbf{C}(s)$. These $n \times n$ matrices (n denotes the number of conductors in the transmission line) are complex and define the relation between the $n \times 1$ vectors of voltage \mathbf{v} and current \mathbf{i} along an infinitesimal distance dx along the line

$$\begin{cases} -\frac{d\mathbf{v}}{dx} = \mathbf{Z}\mathbf{i} \\ -\frac{d\mathbf{i}}{dx} = \mathbf{Y}\mathbf{v} \end{cases} \quad (32)$$

The solution to the wave equation can be expressed in terms of incident and reflected waves at the two line ends (see Fig. 8). In the FD-MD-TLM, a formulation has been adopted based on current waves where the current \mathbf{i}_k at end k is related to the voltage \mathbf{v}_k and the incident current wave \mathbf{i}_{ki} via discretization of the convolutions in time domain

$$\begin{cases} \mathbf{i}_k(t) = Y_c(t) * \mathbf{v}_k(t) + \mathbf{I}_{\text{his},k}(t - \tau) \\ \quad = Y_c(t) * \mathbf{v}_k(t) - 2\mathbf{i}_{ki}(t) \\ \mathbf{i}_{ki}(t) = \mathbf{H}(t) * \mathbf{i}_{mr}(t) \end{cases} \quad (33)$$

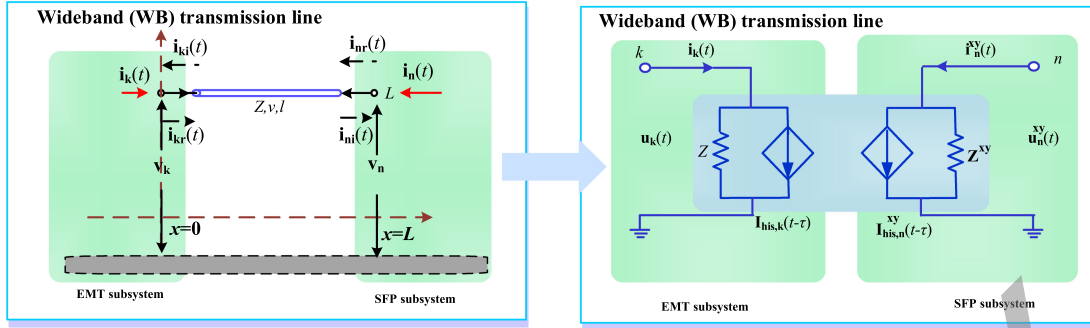


Fig. 8. Structure of the FD-MD-TLM.

where \mathbf{Y}_c and \mathbf{H} are the matrices of characteristic admittance and propagation, respectively; $\mathbf{i}_{ki}(t)$ is the incident current wave; and $\mathbf{i}_{mr}(t)$ is the reflected wave.

The frequency-dependent characteristic impedance \mathbf{Y}_c can be approximated by vector fitting as

$$Y_c = \sum_{i=1}^N \frac{r_i}{s - p_i} \quad (34)$$

where r_i and p_i denote the residues and poles, respectively, and N is the total number.

Consider the convolution of $y_i(t) = h_i(t) * \mathbf{v}_k(t)$ where $h_i(s) = \frac{r_i}{s - p_i}$. $y_i(t)$ can be calculated by transferring the first-order rational function into time domain

$$\begin{aligned} y_i(t) &= r_i e^{p_i \Delta t} y_i(t - \Delta t) + r_i \int_0^{\Delta t} e^{p_i \tau} \mathbf{v}_k(t - \tau) d\tau \\ &= r_i \alpha y_i(t - \Delta t) + r_i \{ \lambda \mathbf{v}_k(t) + \mu \mathbf{v}_k(t - \Delta t) \} \end{aligned} \quad (35)$$

where

$$\alpha = e^{p_i \Delta t}, \lambda = -\frac{1}{p_i} \left(1 + \frac{1 - \alpha}{p_i \Delta t} \right), \mu = -\frac{1}{p_i} \left(\frac{\alpha - 1}{p_i \Delta t} - \alpha \right). \quad (36)$$

Similarly, the frequency-dependent propagation matrix \mathbf{H} can be approximated by different groups of the first-order rational functions with different time delays

$$\mathbf{H} = \sum_{k=1}^{Ng} e^{-sT_k} \sum_{i=1}^{N(k)} \frac{R_{k,i}}{s - p_{k,i}} \quad (37)$$

where T_k is the delay associated with the velocity of the k th mode and Ng is the number of modes; $N(k)$ is the fitting order of the k th term; and $R_{k,i}$ and $p_{k,i}$ represent its k th fitting pole and a matrix of residues determined by a vector fitting process.

Consider the convolution of $\mathbf{y}_i(t) = h_i(t) * \mathbf{i}_{mr}(t)$ where $h_i(s) = \frac{r_i}{s - p_i} e^{-sT}$. $\mathbf{y}_i(t)$ can be calculated by transferring the first-order rational function into time domain

$$\mathbf{y}_i(t) = r_i e^{p_i \Delta t} \mathbf{y}_i(t - \Delta t) + r_i \int_0^{\Delta t} e^{p_i \tau} \mathbf{i}_{mr}(t - \tau - T) d\tau \quad (38)$$

where

$$\begin{cases} \mathbf{x}_i(t) = \alpha \mathbf{x}_i(t - \Delta t) + \lambda \mathbf{i}_{mr} [t - (k + \xi) \Delta t] \\ \quad + \mu \mathbf{i}_{mr} [t - (k + 1 + \xi) \Delta t] \\ \mathbf{y}_i(t) = r_i \mathbf{x}_i(t) \end{cases} \quad (39)$$

where $k = [T/\Delta t]$, $[\cdot]$ is the integer function; and $\xi \in R$, $\xi \in (0, 1)$.

On the other hand, the equivalent model in the SFP subsystem is represented by complex values as

$$\begin{cases} \mathbf{i}_m^{xy}(t) = Y_c(t) * \mathbf{v}_m^{xy}(t) + \mathbf{I}_{his,m}^{xy}(t - \tau) \\ \quad = Y_c(t) * \mathbf{v}_m^{xy}(t) - 2\mathbf{I}_{mi}^{xy}(t) \\ \mathbf{i}_{mi}^{xy}(t) = \mathbf{H}(t) * \mathbf{i}_{kr}^{xy}(t) \end{cases} \quad (40)$$

where $\mathbf{i}_{mi}^{xy}(t)$ is the incident current wave at node m ; $\mathbf{i}_{kr}^{xy}(t)$ is the reflected wave at node k ; and $\mathbf{I}_{his,m}^{xy}(t - \tau)$ is the historic current in xy coordinates.

Similarly, the frequency-dependent characteristic impedance \mathbf{Y}_c can be approximated by vector fitting as

$$Y_c = \sum_{i=1}^N \frac{r_i}{s - p_i} \quad (41)$$

where r_i and p_i denote the residues and poles, respectively, and N is the total number.

Consider the convolution of $K_i^{xy}(t) = h_i(t) * \mathbf{v}_m^{xy}(t)$ where $h_i(s) = \frac{r_i}{s - p_i}$. $K_i^{xy}(t)$ can be calculated by transferring the first-order rational function into time domain and transferring $\mathbf{v}_m^{xy}(t)$ into its shifted phasor form

$$\begin{aligned} K_i^{xy}(t) &= r_i e^{p_i \Delta t} K_i^{xy}(t - \Delta t) + r_i \int_0^{\Delta t} e^{p_i \tau} \mathbf{v}_m^{xy}(t - \tau) d\tau \\ &= r_i e^{p_i \Delta t} K_i^{xy}(t - \Delta t) + r_i e^{j\omega_s t} \\ &\quad \times \int_0^{\Delta t} e^{(p_i - j\omega_s)\tau} \hat{\mathbf{v}}_m^{xy}(t - \tau) d\tau. \end{aligned} \quad (42)$$

Performing the integration by parts, (42) is expanded and recast as follows:

$$K_i^{xy}(t) = r_i e^{p_i \Delta t} K_i^{xy}(t - \Delta t) + \frac{r_i [e^{p_i \Delta t} \hat{\mathbf{v}}_m^{xy}(t - \Delta t) - \hat{\mathbf{v}}_m^{xy}(t)]}{p_i - j\omega_s} - \frac{r_i}{p_i - j\omega_s} e^{j\omega_s t} \int_0^{\Delta t} e^{(p_i - j\omega_s)\tau} \frac{d\hat{\mathbf{v}}_m^{xy}(t - \tau)}{dt} d\tau \quad (43)$$

where

$$\frac{d\hat{\mathbf{v}}_m^{xy}(t - \tau)}{dt} = \frac{\hat{\mathbf{v}}_m^{xy}(t - \tau) - \hat{\mathbf{v}}_m^{xy}(t)}{\tau} = \frac{e^{-j\omega_s t}}{\tau} [e^{j\omega_s \tau} \mathbf{v}_m^{xy}(t - \tau) - \mathbf{v}_m^{xy}(t)]. \quad (44)$$

Substituting (44) in (43), rearrangement and simplification lead to

$$K_i^{xy}(t) = r_i e^{p_i \Delta t} K_i^{xy}(t - \Delta t) + \frac{r_i [e^{p_i \Delta t} \mathbf{v}_m^{xy}(t - \Delta t) - \mathbf{v}_m^{xy}(t)]}{p_i - j\omega_s} - \frac{r_i}{(p_i - j\omega_s) \Delta t} [e^{j\omega_s \tau} \mathbf{v}_m^{xy}(t - \Delta t) - \mathbf{v}_m^{xy}(t)] A, A = \int_0^{\Delta t} e^{(p_i - j\omega_s)\tau} d\tau. \quad (45)$$

Similarly, the frequency-dependent propagation matrix \mathbf{H} can be approximated by different groups of the first-order rational functions with different time delays according to (37). Consider the convolution of $\mathbf{i}_{mi}^{xy}(t) = h_i(t) * \mathbf{i}_{kr}^{xy}(t)$ where $h_i(s) = \frac{r_i}{s - p_i} e^{-sT}$. $\mathbf{i}_{mi}^{xy}(t)$ can be calculated by transferring the first-order rational function into time domain and transferring $\mathbf{i}_{kr}^{xy}(t)$ into its shifted phasor form

$$\mathbf{i}_{mi}^{xy}(t) = r_i e^{p_i \Delta t} \mathbf{i}_{mi}^{xy}(t - \Delta t) + r_i \int_0^{\Delta t} e^{p_i \tau} \mathbf{i}_{kr}^{xy}(t - \tau - T) d\tau = r_i e^{p_i \Delta t} \mathbf{i}_{mi}^{xy}(t - \Delta t) + r_i e^{j\omega_s(t-T)} \times \int_0^{\Delta t} e^{(p_i - j\omega_s)\tau} \mathbf{i}_{kr}^{xy}(t - \tau - T) d\tau. \quad (46)$$

Performing the integration by parts, (46) is expanded and recast as follows:

$$\mathbf{i}_{mi}^{xy}(t) = r_i e^{p_i \Delta t} \mathbf{i}_{mi}^{xy}(t - \Delta t) + \frac{r_i e^{-j\omega_s T} [e^{p_i \Delta t} \hat{\mathbf{i}}_{kr}^{xy}[t - (k+1+\xi)\Delta t] - \hat{\mathbf{i}}_{kr}^{xy}[t - (k+\xi)\Delta t]]}{p_i - j\omega_s} - \frac{r_i}{p_i - j\omega_s} e^{j\omega_s(t-T)} \int_0^{\Delta t} e^{(p_i - j\omega_s)\tau} \frac{d\hat{\mathbf{i}}_{kr}^{xy}(t - \tau)}{dt} d\tau \quad (47)$$

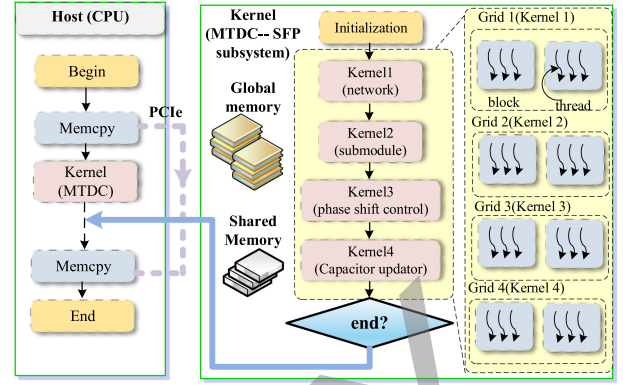


Fig. 9. Flowchart of simulations of SFP subsystems on GPU using dynamic parallelism.

where

$$\frac{d\hat{\mathbf{i}}_{kr}^{xy}(t - \tau)}{dt} = \frac{\hat{\mathbf{i}}_{kr}^{xy}(t - \tau) - \hat{\mathbf{i}}_{kr}^{xy}(t)}{\tau} = \frac{e^{-j\omega_s t}}{\tau} [e^{j\omega_s \tau} \hat{\mathbf{i}}_{kr}^{xy}(t - \tau) - \hat{\mathbf{i}}_{kr}^{xy}(t)]. \quad (48)$$

Substituting (48) in (47), rearrangement and simplification lead to

$$\mathbf{i}_{mi}^{xy}(t) = r_i e^{p_i \Delta t} \mathbf{i}_{mi}^{xy}(t - \Delta t) + \frac{r_i e^{-j\omega_s T} [e^{p_i \Delta t} \hat{\mathbf{i}}_{kr}^{xy}[t - (k+1+\xi)\Delta t] - \hat{\mathbf{i}}_{kr}^{xy}[t - (k+\xi)\Delta t]]}{p_i - j\omega_s} - \frac{r_i}{(p_i - j\omega_s) \Delta t} e^{-j\omega_s T} \times [e^{j\omega_s \tau} \hat{\mathbf{i}}_{kr}^{xy}[t - (k+1+\xi)\Delta t] - \hat{\mathbf{i}}_{kr}^{xy}[t - (k+\xi)\Delta t]] B B = \int_0^{\Delta t} e^{(p_i - j\omega_s)\tau} d\tau. \quad (49)$$

C. Massively Parallel Implementation on Integrated CPU-GPUs

As claimed, the MMCs are the most time-consuming component of the large-scale ac-dc grids. In order to improve the efficiency, the simulations of the SFP subsystem, which is mainly composed of several MMCs, are realized on many-core GPUs (see Fig. 9). Generally, two ways are adopted to accelerate the simulation speed of GPU-based simulations: 1) reduce the communication between CPUs and GPUs; and 2) increase the parallelism of GPU programs. As a result, control and state variables of the whole system are first initialized, and then the calculations of the SFP subsystem are purely done on GPUs. In order to increase the parallelism of GPU programs, the whole system is updated at the submodule level and the computation is separated as several kernels, such as the network solver kernel and the submodule kernel. Specifically, the calculations of the capacitor voltages and the update of the Thevenin equivalent of each submodule can be calculated in an independent and parallel way, each of which can be realized as a single kernel function. Here, each kernel function is computed in a grid of a

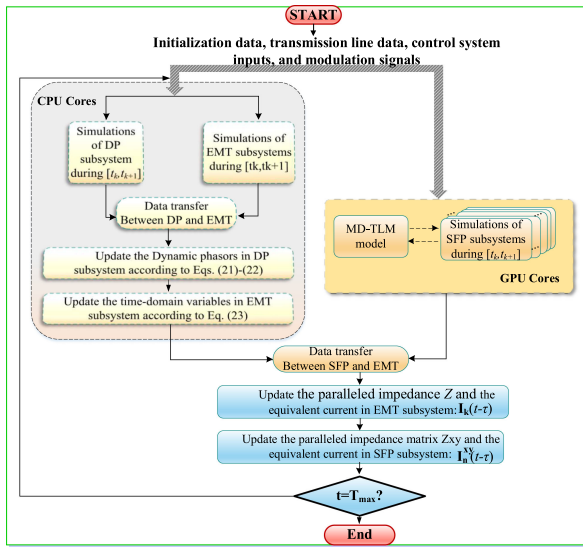


Fig. 10. Overall procedure of the proposed cosimulation method in integrated CPU-GPUs.

blocks each of which having b threads, meaning a total number of $a \times b$ copies can be launched simultaneously.

The overall procedure of the cosimulation method is shown in Fig. 10. First, the whole system is partitioned into the SFP subsystem, DP subsystem, and EMT subsystem, respectively. The large-scale ac grids are contained in the EMT subsystem, the LCC is included in the DP subsystem, and the MMCs are included in the SFP subsystem. Both the DP and the EMT subsystems are implemented in CPU cores, where their interactions are reflected by controlled voltage and current circuits in the form of DPs. The calculations of the SFP subsystem are realized in the many-core GPU cores, and the interactions between the SFP subsystem and other subsystems are reflected by the proposed MD-TLM model. Finally, as the total simulation time (T_{\max}) is reached, the cosimulation comes to an end and all results are output to the users.

V. NUMERICAL TESTS AND VALIDATIONS

In this section, the proposed cosimulation method of SFP/DP and EMT models, which is implemented on integrated CPU-GPUs, is applied to a practical ac-dc system in China (see Fig. 11). For the LCC- and MMC-based MTdc grid, Converters T1-T3 adopt the MMC (half-bridge, full-bridge, and CDSM) topology and Converter T4 adopts the LCC topology. In the MTdc grid, Converter 1 is responsible for maintaining constant dc voltage, whereas other converters control the power flow. If not specially mentioned, the simulation time steps of different subsystems of our proposed method are set as $20 \mu\text{s}$, respectively. Meanwhile, simulation results obtained with a unanimous time step of $20 \mu\text{s}$ by PSCAD/EMTDC are used as the high-fidelity reference values.

A. Converter-Level Test 1

In this section, the accuracy and efficiency of the SFP subsystem is compared with the reference result. The simulation scenario is the output voltage of Converter 1 under different

levels. As shown in Fig. 12, the simulation results of the proposed method match the reference curve very closely, especially the proposed method has satisfied the accuracy expectations concerning the voltage spikes of lower levels.

In Table I, the execution time and speedup of detailed model by PSCAD, efficient SFP model on CPUs/GPUs are compared. As can be seen, the GPU results overtake the CPU results when the MMC level reaches 11 or more. When the MMC level reaches 65, the GPU results have achieved a speedup of 171 compared to the detailed model in PSCAD, showing its advantages in improving the efficiency. Moreover, the execution time of update of Norton equivalents is much larger than that of solving nodal voltage equation for both CPUs and GPUs.

The efficiency improvement of MMCs on GPUs is due to the following reasons. First, based on the model reduction technique, the calculation of the MMC by our SFP model is derived as a two-stage model. The first stage is to calculate the global node voltage equation, where each arm of the MMC is represented by one Norton equivalent circuit according to (16) and (17). Therefore, the number of nodes will not expand as the number of submodules increases, and only one node will be added in the node voltage equations. This node is the connecting node between upper and lower arms. In the second stage, the capacitor voltages are refreshed in a parallel and independent way [see (9)], which, taking the real and imaginary parts into account, is only a two-dimensional equation and thus can be very efficiently worked out. Second, as the quantities at the submodule level by our proposed SFP-based MMC model can be calculated independently, the proposed model is most suitable to utilize the many-core GPUs to increase the parallelism of calculations for the MMCs. Specifically, the update of the Thevenin equivalent circuit of each submodule and the update of the capacitor voltage of each submodule can be realized as different kernel functions of GPUs.

B. Converter-Level Test 2: The AC-Side Energization of the MMC

The comparative results of capacitor voltages for the MMC T1 during the ac side energization are given in Fig. 13. As can be seen, the MMC T1 is precharged since $t = 0.1 \text{ s}$, where all the submodules are blocked. Until $t = 0.3 \text{ s}$, the precharged process is finished and the sum of capacitor voltages in each arm equals to $1.732 V_m$, where V_m refers to the peak value of phase-to-phase ac voltage. After $t = 0.3 \text{ s}$, capacitor voltages are recharged to their preset values. Concerning the accuracy during the precharged process, the proposed method overlaps with the reference curve. Especially, as shown in zoomed-in figures, capacitor voltage of each submodule exactly matches that of the reference curve.

C. Universality of the Proposed SFP-Based MMC Model

In order to show the universality of the proposed model, the basic element of the alternate arm converter (AAC) is given as an example, as shown in Fig. 14. All the switches are represented as the controlled conductance, such as G_{ei}^{xy} , $i = 1, 2, \dots, 4$, whereas the capacitor is represented as the SFP-based Norton equivalents, i.e., G_c^{xy} and $J_c^{xy}(t - \Delta t)$.

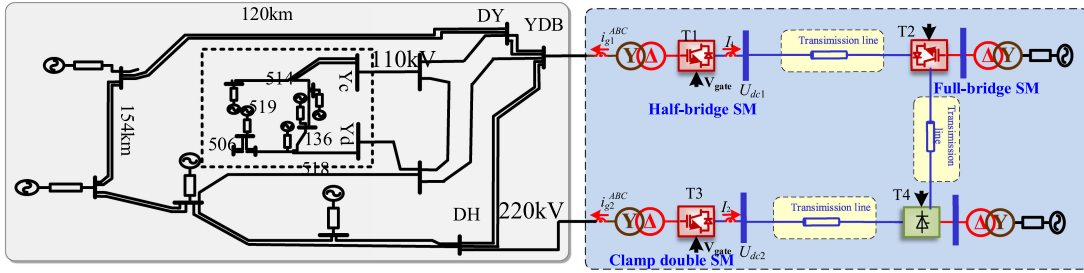


Fig. 11. Practical ac-dc system in China integrating the LCC- and MMC-based MTdc grid.

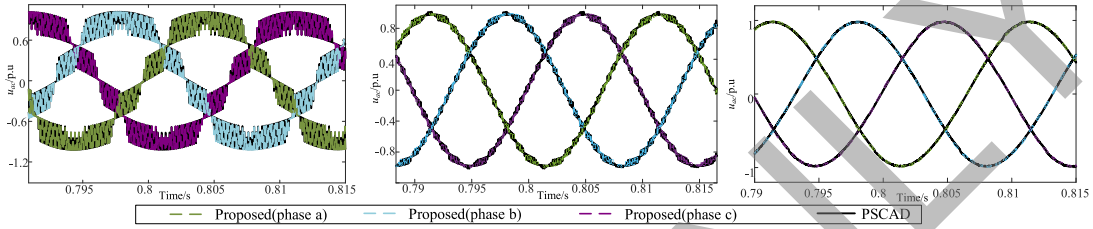


Fig. 12. Accuracy comparisons of Converter 1 on different levels (five levels, 17 levels, and 65 levels).

TABLE I
MMC-BASED CONVERTER 1 EXECUTION TIME BY VARIOUS PLATFORM FOR 2-S DURATION

MMC Level	Execution Time(s)					Speed-up	
	PSCAD	CPU		GPU		SP_{CPU}	SP_{GPU}
5-L	28	0.95	4.25	2.5	5.1	5.4	3.7
11-L	61.2	8.1	27.1	8.1	2	1.7	6
21-L	297.8	15.4	52.4	12	2.3	4.4	20.8
65-L	2809.7	31	131	13.8	2.6	17.3	171

T1 (task 1): represents the time cost of solving nodal voltage equations.

T2 (task 2): represents the time cost of calculating Norton equivalents of each electrical component.

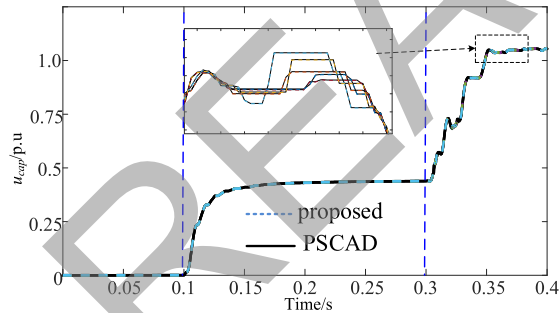


Fig. 13. Capacitor voltages of the MMC T1 during the ac side energization.

According to Steps 1 and 2 in Section II-B, the incidence vector, which reflects the connected buses of the component, is derived. For example, for the switch S1, the incidence vector M_1 is given as

$$M_1 = [1 \ 0 \ -1 \ 0 \ 0]^T. \quad (50)$$

Similarly, the nodal voltage equation of the whole system in Fig. 13 can be formulated according to Step 2 as in Fig. 15.

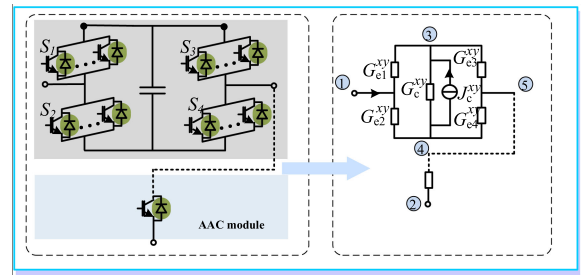


Fig. 14. Structure of the AAC module.

$$\begin{bmatrix} G_{e1}^{xy} + G_{e2}^{xy} & 0 & -G_{e1}^{xy} + G_{e3}^{xy} & -G_{e2}^{xy} & -G_{e3}^{xy} - G_{e5}^{xy} \\ 0 & G_{e5}^{xy} & 0 & 0 & 0 \\ G_{e1}^{xy} & 0 & G_{e1}^{xy} & 0 & 0 \\ -G_{e2}^{xy} & 0 & 0 & G_{e2}^{xy} + G_{e4}^{xy} & -G_{e4}^{xy} \\ 0 & -G_{e5}^{xy} & -G_{e3}^{xy} & -G_{e4}^{xy} & G_{e3}^{xy} + G_{e4}^{xy} + G_{e5}^{xy} \end{bmatrix} \begin{bmatrix} v_1^{xy}(t) \\ v_2^{xy}(t) \\ v_3^{xy}(t) \\ v_4^{xy}(t) \\ v_5^{xy}(t) \end{bmatrix} = \begin{bmatrix} J_B^{xy}(t-\Delta t) \\ 0 \\ J_C^{xy}(t-\Delta t) \\ -J_C^{xy}(t-\Delta t) \\ J_N^{xy}(t-\Delta t) \end{bmatrix}$$

Fig. 15. Structure of nodal voltage equation of the AAC module.

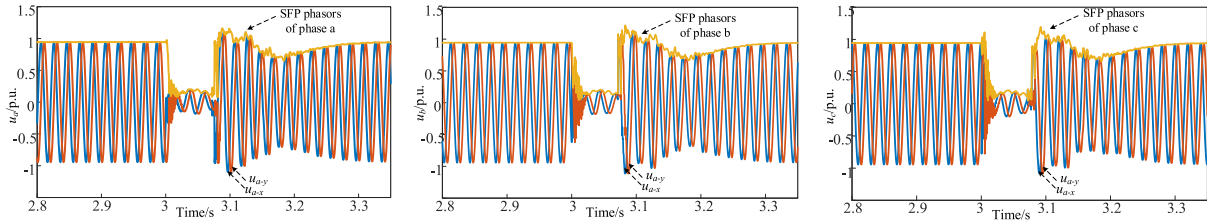


Fig. 16. Instantaneous and SFP curves of the ac currents at Bus DH.

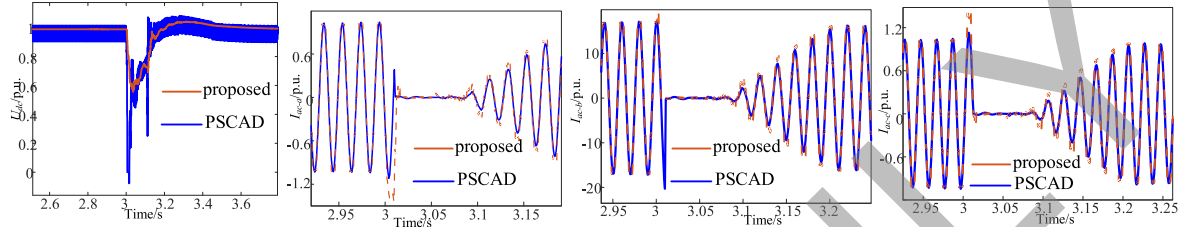


Fig. 17. DC voltage and ac currents of the LCC converter.

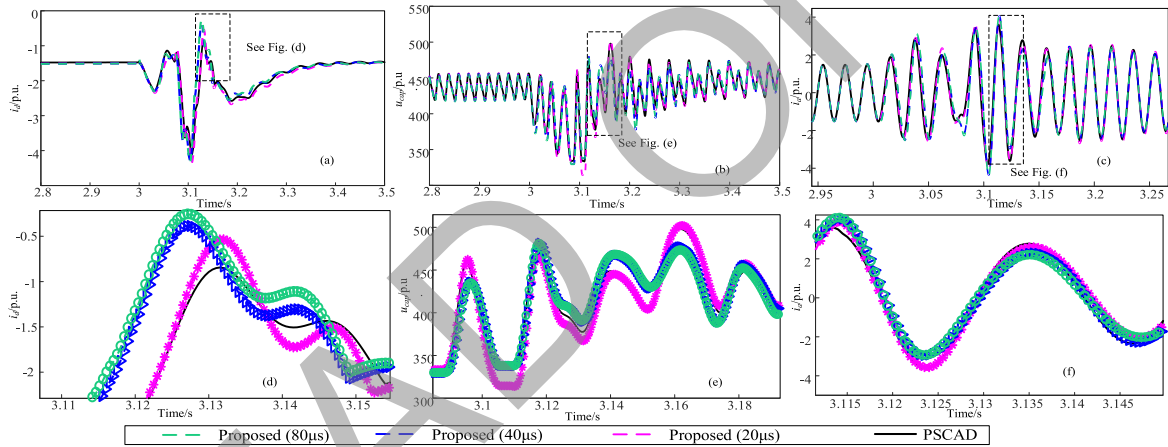


Fig. 18. Simulation results/errors of dc currents, capacitor voltages (phase A), and ac currents (phase A) of Station 3.

The final SFP-based Norton equivalents can be obtained by Gaussian elimination

$$\begin{cases} G_{eq} = G_{BB}^{xy} - G_{BN}^{xy} [G_{NN}^{xy}]^{-1} G_{NB}^{xy} \\ \mathbf{J}_{eq}^{xy}(t - \Delta t) = \mathbf{J}_B^{xy}(t - \Delta t) - G_{BN}^{xy} [G_{NN}^{xy}]^{-1} \mathbf{J}_N^{xy}(t - \Delta t) \end{cases} \quad (51)$$

D. System-Level Test 1: An AC Resistive Fault

In this scenario, the fault is triggered at Bus DH at $t = 3.0$ s and the fault is cleared 80 ms later. Bus DH is the interface bus between the MTdc grid and the adjacent ac grid. Fig. 16 displays the instantaneous and SFP curves of the ac voltages. Clearly, the SFP curves match the envelopes of instantaneous values exactly. The simulation results also demonstrate that different types of oscillations exist in the system: 1) the high-frequency electromagnetic oscillations aroused by the frequency-dependent dynamics of transmission lines. This process only lasts for one or two cycles following the disturbances. 2) The sustained low-

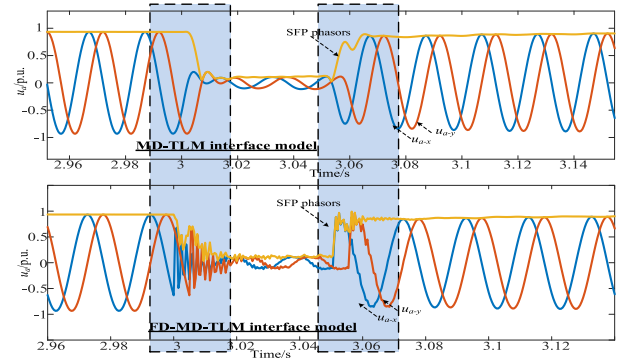


Fig. 19. Comparisons of interface ac voltages based on MD-TLM/FD-MD-TLM model.

frequency oscillations of small amplitude after the clearance of the fault, which are aroused by the power swings of generators and converters. Figs. 17 and 18 show the simulation results

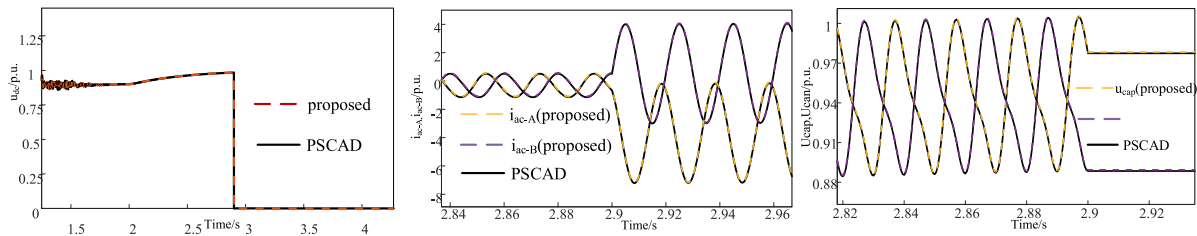


Fig. 20. DC voltage, ac currents, and capacitor voltages of the T1 (HBSM).

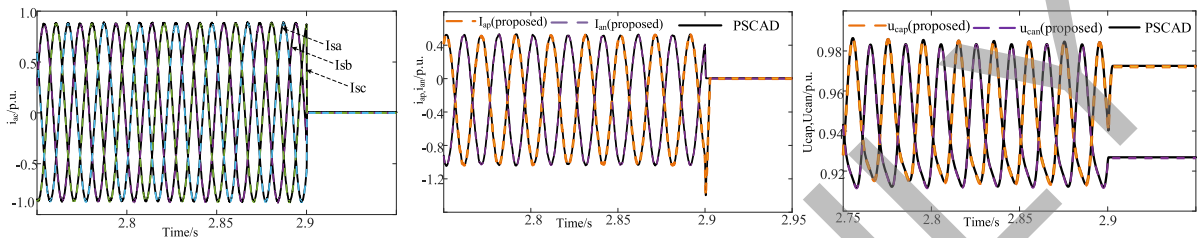


Fig. 21. AC currents, arm current, and capacitor voltages of the T3 (CDSM).

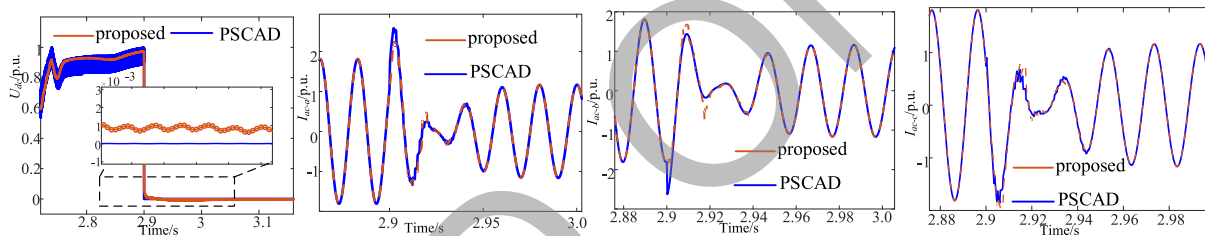


Fig. 22. DC voltage and ac currents of the LCC converter.

of the LCC and the MMC, respectively. Their results indicate that the efficient models in SFP and DP subsystems can satisfy the accuracy expectations. Especially, when the time step is extended to $80 \mu\text{s}$, the SFP model can still achieve a quite satisfied precision, which is clearly demonstrated by the zoomed-in curves in Fig. 18(d)–(f).

E. Discussion on the MD-TLM and the FD-MD-TLM Between SFP and EMT Subsystems

The comparisons of interface ac voltages based on different interface models between SFP and EMT subsystems are detailed in Fig. 19. The following conclusions can be reached: 1) the interface model between SFP and EMT subsystems, regardless of the MD-TLM or the FD-MD-TLM model, can give wide frequency band phasor and instantaneous values simultaneously, where the phasors are the exact envelopes of the instantaneous values at all occasions; and 2) the FD-MD-TLM model can reflect the high-frequency dynamics of interfacing, whereas the MD-TLM model fails.

F. System-Level Test 2: A DC Pole-to-Pole Fault

A dc pole-to-pole permanent fault is triggered at the dc bus between Converters T3 and T4 from $t = 2.9 \text{ s}$. DC voltages, ac

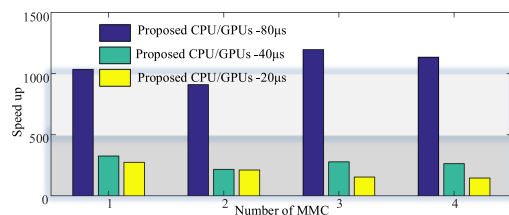


Fig. 23. Speedup of the proposed method on CPUs/GPUs for different number of converters.

currents, and capacitor voltages of the MMC T1 (HBSM) are depicted in Fig. 20; ac currents, arm current, and capacitor voltages of the T3 (CDSM) are given in Fig. 21; and dc voltages and ac currents of the LCC are depicted in Fig. 22. As demonstrated, simulation results of the MMC and the LCC both match the reference curve very well. As shown in Fig. 21, since CDSM MMC can block the dc pole-to-pole fault, the ac currents are suppressed. As shown in the zoomed-in figures in Fig. 22, the errors between the proposed model and the reference curve by PSCAD/EMTDC can be as small as $1\text{e}-3 \text{ p.u.}$, which shows that the proposed method can achieve quite a satisfied accuracy. That is to say, accuracy of both the SFP and DP subsystems is guaranteed by our proposed interface models under dc fault scenarios.

TABLE II

COMPARISONS OF EXECUTION FOR DIFFERENT NUMBER OF CONVERTERS

Converter number	Execution Time(s)			
	PSCAD	Proposed (CPU/GPU) under different time-steps/s		
		20	40	80
1	1×10^4	36.7	30.8	9.7
2	1.1×10^4	64.1	52.9	12.6
3	1.8×10^4	114.5	63.3	14.7
4	2.2×10^4	154.4	85.4	19.8

G. Comparisons of Simulation Efficiency

In this article, the simulation efficiency is measured in terms of execution time and speedup (see Table II and Fig. 23). The speedup is defined as the ratio of the execution time consumed by PSCAD (base scenario) and the proposed method. Note that the time step of PSCAD models is restricted to 20 μ s to guarantee numerical stability of the simulation. The GPU used in this article is the Nvidia Titan E5-2650V4 with 5120 CUDA cores and 64 GB RAM. As can be seen, the execution time of the proposed method is much lower than PSCAD. The speedup is evident, especially when the time step of the proposed method is extended to 80 μ s. As the scale of system or number of MMCs increases to 4, the speedup grows as a whole, achieving a speedup of 1e3 times. In summary, the efficiency improvement is due to the following reasons.

- 1) The simulation efficiency of the SFP subsystem is greatly improved by three techniques, or adopting a much larger time step, model order reduction technique, and the many-core GPU acceleration.
- 2) The efficiency of simulations of the LCC is improved by DP modeling.
- 3) The simulation efficiency of the whole system is further improved by the proposed cosimulation structure, based on the respective SFP/DP and EMT models, among which their interactions are reflected by the proposed interface models and the time sequences of simulations are governed by the overall procedure.

Therefore, the proposed method has improved the efficiency significantly in simulating the large-scale ac–dc grids while guaranteeing the accuracy expectations.

VI. CONCLUSION

In order to capture detailed dynamics and their interactions of large-scale ac–dc systems integrating LCC- and MMC-based MTdc grids, an accurate and efficient simulation method is highly necessary. In this article, a cosimulation method based on integrated CPU–GPUs was proposed where the target system is decoupled into the SFP subsystem, the DP subsystem, and the EMT subsystem, respectively. The MMCs were included in the GPU-based SFP subsystem and the LCCs were included in the CPU-based DP subsystem. The majority of the ac grids were included in the EMT subsystem. The interactions between SFP/DP and EMT subsystems were reflected by the so-called interface models, or the MD-TLM and the controlled current and voltage circuits. The overall cosimulation method was real-

ized by the respective SFP/DP and EMT models, among which their interactions were reflected by the proposed interface models and the time sequences of simulations were governed by the overall procedure. The performance of the proposed method was validated on a practical large-scale ac–dc system, which demonstrated that the following conditions hold.

- 1) The phasor curves obtained by the SFP models match the envelopes of instantaneous values exactly. The SFP instantaneous values match the reference curves by EMT models exactly.
- 2) The DP-based LCC model can preserve the accurate dynamic responses compared to the detailed EMT models.
- 3) The overall cosimulation method on integrated CPU–GPUs achieved significant speedup when the time step extended over 50 μ s.

REFERENCES

- [1] X. Chen *et al.*, “Integrating wind farm to the grid using hybrid multiterminal HVDC technology,” *IEEE Trans. Ind. Appl.*, vol. 47, no. 2, pp. 965–972, Mar./Apr. 2011.
- [2] R. Teixeira Pinto, P. Bauer, S. F. Rodrigues, E. J. Wiggelinkhuizen, J. Pierik, and B. Ferreira, “A novel distributed direct voltage control strategy for grid integration of offshore wind energy systems through MTdc network,” *IEEE Trans. Ind. Electron.*, vol. 60, no. 6, pp. 2429–2441, Jun. 2013.
- [3] C. Qi *et al.*, “A decentralized optimal operation of AC/DC hybrid distribution grids,” *IEEE Trans. Smart Grid*, vol. 9, no. 6, pp. 6095–6105, Nov. 2018.
- [4] D. Shu, X. Xie, H. Rao, X. Gao, Q. Jiang, and Y. Huang, “Sub- and super-synchronous interactions between STATCOMs and weak AC/DC transmissions with series compensations,” *IEEE Trans. Power Electron.*, vol. 33, no. 9, pp. 7424–7437, Sep. 2018.
- [5] J. Peralta, H. Saad, S. Denetiere, J. Mahseredjian, and S. Nguefeu, “Detailed and averaged models for a 401-level MMC-HVDC system,” *IEEE Trans. Power Del.*, vol. 27, no. 3, pp. 1501–1508, Jul. 2012.
- [6] U. N. Gnanarathna, A. M. Gole, and R. P. Jayasinghe, “Efficient modeling of modular multilevel HVDC converters (MMC) on electromagnetic transient simulation programs,” *IEEE Trans. Power Del.*, vol. 26, no. 1, pp. 316–324, Jan. 2011.
- [7] N. R. Chaudhuri, B. Chaudhuri, R. Majumder, and A. Yazdani, *Multiterminal Direct-Current Grids: Modeling, Analysis, and Control*. Hoboken, NJ, USA: Wiley, 2014.
- [8] M. Daryabak *et al.*, “Modeling of LCC-HVDC systems using dynamic phasors,” *IEEE Trans. Power Del.*, vol. 29, no. 4, pp. 1989–1998, Aug. 2014.
- [9] C. Liu, A. Bose, and P. Tian, “Modeling and analysis of HVDC converter by three-phase dynamic phasor,” *IEEE Trans. Power Del.*, vol. 29, no. 1, pp. 3–12, Feb. 2014.
- [10] K. Mudunkotuwa, S. Filizadeh, and U. Annakkage, “Development of a hybrid simulator by interfacing dynamic phasors with electromagnetic transient simulation,” *IET Gener., Transmiss. Distrib.*, vol. 11, no. 12, pp. 2991–3001, 2017.
- [11] S. Rajesvaran and S. Filizadeh, “Modeling modular multilevel converters using extended-frequency dynamic phasors,” in *Proc. IEEE Power Energy Soc. Gen. Meeting*, 2016, pp. 1–5.
- [12] Z. Zhou and V. Dinavahi, “Parallel massive-thread electromagnetic transient simulation on GPU,” *IEEE Trans. Power Del.*, vol. 29, no. 3, pp. 1045–1053, Jun. 2014.
- [13] P. Li, X. Fu, C. Wang, H. Yu, D. Lin, and F. Xing, “Matrix exponential based algorithm for electromagnetic transient modeling and simulation of large-scale induction generator wind farms,” in *Proc. IEEE Power Energy Soc. Gen. Meeting*, Denver, CO, USA, 2015.
- [14] G. Geng, Q. Jiang, and Y. Sum, “Parallel transient stability-constrained optimal power flow using GPU as coprocessor,” *IEEE Trans. Smart Grid*, vol. 8, no. 3, pp. 1436–1445, May 2017.
- [15] D. Shu and X. Xie *et al.*, “A multi-domain co-simulation method for comprehensive shifted-frequency phasor DC-grid models and EMT AC-grid models,” *IEEE Trans. Power Syst. Electronics*, vol. 34, no. 1, pp. 10557–10574, Feb. 2019.

- [16] P. Zhang, J. R. Marti, and H. W. Dommel, "Induction machine modelling based on shifted frequency analysis," *IEEE Trans. Power Syst.*, vol. 24, no. 1, pp. 157–164, Feb. 2009.
- [17] D. Shu, V. Dinavahi, X. Xie, and Q. Jiang, "Shifted frequency modeling of hybrid modular multilevel converters for simulation of MTdc grid," *IEEE Trans. Power Del.*, vol. 33, no. 3, pp. 1288–1298, Jun. 2018.
- [18] X. Wang, *Modern Power Systems Analysis*. New York, NY, USA: Springer, 2008.



Dewu Shu (M'18) received the B.Sc. and Ph.D. degrees in electrical engineering from Tsinghua University, Beijing, China, in 2013 and 2018, respectively.

He is currently the Tenure-Track Assistant Professor in electrical engineering with Shanghai Jiao Tong University, Shanghai, China. His research interests include multirate EMT/TS simulations, and parallel and distributed computing.



Yingdong Wei (M'xx) was born in Henan Province, China, in 1979. He received the B.S. and M.S. degrees from the College of Electrical Engineering, Zhejiang University, Hangzhou, China, in 2002 and 2005, respectively, and the Ph.D. degree from the Department of Electrical Engineering, Tsinghua University, Beijing, China, in 2009.

In 2011, he joined Tsinghua University, where he is currently a Research Associate. His research interests include hybrid ac–dc power system and traction power system.



Venkata Dinavahi (S'94–M'00–SM'08) received the B.Eng. degree in electrical engineering from the Visvesvaraya National Institute of Technology, Nagpur, India, in 1993, the M.Tech. degree in electrical engineering from the Indian Institute of Technology Kanpur, Kanpur, India, in 1996, and the Ph.D. degree in electrical and computer engineering from the University of Toronto, Toronto, ON, Canada, in 2000.

He is currently a Professor with the Department of Electrical and Computer Engineering, University of Alberta, Edmonton, AB, Canada. His research interests include real-time simulation of power systems and power electronic systems, electromagnetic transients, device-level modeling, large-scale systems, and parallel and distributed computing.



Keyou Wang (S'05–M'09) received the B.S. and M.S. degrees in electrical engineering from Shanghai Jiao Tong University, Shanghai, China, in 2001 and 2004, respectively, and the Ph.D. degree from the Missouri University of Science and Technology (formerly University of Missouri-Rolla), Rolla, MO, USA, in 2008.

He is currently an Associate Professor and the Vice Department Chair of Electrical Engineering with Shanghai Jiao Tong University. His research interests include power system dynamics and stability, renewable energy integration, and converter dominated power system.

Dr. Wang is an Associate Editor for *IET Generation Transmission and Distribution*.



Zheng Yan (M'98) received the B.S. degree from Shanghai Jiao Tong University, Shanghai, China, in 1984 and the M.S. and Ph.D. degrees from Tsinghua University, Beijing, China, in 1987 and 1991, respectively, all in electrical engineering.

He is currently a Tenure Professor of Electrical Engineering with Shanghai Jiao Tong University. His research interests include application of optimization theory to power systems, power markets, and dynamic security assessment.



Xiaoqian Li (M'13) was born in Hebei Province, China, in 1987. She received the B.S. degree from North China Electric Power University, Beijing, China, in 2010 and the Ph.D. degree from Tsinghua University, Beijing, China, in 2015, both in electrical engineering.

During 2015 to 2017, she had a postdoctoral position with the Department of Electrical Engineering, Tsinghua University, where she has been an Assistant Professor since 2017. Her research interests include high-power electronic, flexible ac transmission system, and voltage source converter-high-voltage direct current system.